Energetics of a bouncing drop: coefficient of restitution, bubble entrapment and escape

Praveen K. Sharma[1] and Harish N. Dixit[1, a)]

Department of Mechanical & Aerospace Engineering,

Indian Institute of Technology Hyderabad, Kandi, Sangareddy 502285,

India

(Dated: 14 October 2020)

Drops bouncing on an ultra-smooth solid surface can either make contact with the surface or be supported on a thin cushion of gas. If the surface is superhydrophobic, either complete or partial rebound usually occurs. Recent experiments have shed light on the lubrication effect of the underlying gas layer at the onset of impact. Using axisymmetric direct numerical simulations, we shed light on the energetics of a drop bouncing from a solid surface. A complete energy budget of the drop and the surrounding gas during one complete bouncing cycle reveals complex interplay between various energies that occur during impact. Using a parametric study, we calculate the coefficient of restitution as a function of Reynolds and Weber numbers and the results are in good agreement with reported experiments. Our simulations reveal that Weber number and not Reynolds number has a stronger effect on energy losses as the former affects the shape of the drop during impact. At higher Weber and Reynolds numbers, a tiny gas bubble gets trapped inside the drop during impact. We show that a large amount of dissipation occurs during bubble entrapment and escape process. Finally, analysis of the flow field in the underlying gas layer reveals that maximum dissipation occurs in this layer and a simple scaling law is derived for dissipation that occurs during impact.

a)Electronic mail: hdixit@mae.iith.ac.in

Keywords: Drop impact, Energy budget, Surface tension, Lubrication

I. INTRODUCTION

Understanding the dynamics of drop impact near a solid surface offers insights into a diverse range of applications ranging from ink-jet printing[1,2] to heat transfer through spray cooling[3]. Excellent reviews by Yarin[4] and Josserand & Thoroddsen[5] cover many aspect of drop impact dynamics. In the last two decades a number of new and surprising discoveries have been made starting with the seminal work of Xu *et al.*[6] who showed that pressure of the surrounding gas plays a crucial role during the splashing process. This discovery prompted Mandre *et al.*[7] and Mani *et al.*[8] to develop a theory to examine the role of gas and lubrication effects near the solid surface at the onset of impact. Experiments by Kolinski *et al.*[9] indeed found that drop tends to skate on a thin layer of gas before touchdown. Another important discovery made in recent years is that drops can bounce on a smooth surface without ever making contact with it[10,11]. A thin layer of gas cushions the impact and lubrication pressure provides the necessary repulsion force for the drop to bounce back. Using interferometric techniques, de Ruiter *et al.*[11,12] characterised the gas film beneath the drop in great detail and showed that gas films of thickness in the micrometer and nanometer range is trapped beneath the drop.

In a companion paper, we recently conducted an exhaustive numerical study of a drop impacting a solid surface assuming the gas to be incompressible[13] and key results of this work is briefly summarized below. Through a parametric study, the simulations revealed that wettability-independent (WI) or non-contact bouncing and wettability-dependent (WD) or bouncing with contact are separated by a transition boundary in the $We-Re$ plane. The simulations also revealed that WI bouncing is favoured at low Re for a wide range of Weber numbers. In such cases, the drop spreads on a thin layer of gas beneath it. Kolinski *et al.*[10] noted that large shear rates generated in this gas layer can lead to excessive dissipation reducing the coefficient of restitution, always below 0.65 in their experiments, in spite of the low viscosity of air. In contrast, Richard & Quéré[14] report a coefficient of restitution close to 0.9 for a drop bouncing on a superhydrophobic surface. Such a large value in their experiments was attributed to very short contact times during which dissipation is negligible. The results of Kolinski *et al.* is also in contrast to similar experiments by de Ruiter *et al.*[11] who reported a very high coefficient of restitution of 0.96 ± 0.04. Using careful estimation of the energy budget for a wide range of We and Re, we show later that the apparent discrepancy in the coefficient of restitution between Kolinski *et al.*[10] and de Ruiter *et al.*[15] can be resolved by examining the role of Weber and Reynolds numbers. To determine the coefficient of restitution (r_c) accurately, it is necessary to precisely compute the energy budget of a drop during a bouncing event. Closely connected to r_c is the contact time, τ, which is defined as the duration for which the drop stays in *contact* with the solid surface.

For water drops of about 1 mm at moderate impact velocities typically in the range of 0.2 to 2 m/s, Richard *et al.*[16] show that contact time scales with radius of the drop as $\tau \sim R^{3/2}$, obtained by balancing inertia of the drop with surface tension and is independent of velocity. Okumura *et al.*[17] showed that drop deformation and contact time depends on a delicate balance of inertia, gravity and surface tension. At lower impact velocities, they show that contact time increases with decreasing velocity and drop deformation scales as $We^{1/2}$. A more sophisticated quasi-static model of drop impact was developed by Moláček & Bush[18] who showed that contact time and coefficient of restitution depend on both Weber and Ohnesorge numbers.

Understanding the energetics of drop impact also helps determine the radial extent of drop spreading upon impact. Kim & Chun[19] performed experiments using a variety of drop and solid combinations to study spreading and recoiling dynamics. They used an empirically determined dissipation factor to account for viscous dissipation during drop spreading and found that increasing Weber number promotes faster recoil. Not surprisingly, drops with large equilibrium contact angle were found to have very short contact times, a result consistent with the finding of Richard *et al.*[14]. For drops bouncing on superhydrophobic surfaces at higher Weber numbers, contact dissipation may be small, but such drops undergo pronounced oscillations after lift-off which generates vigorous motion inside the drop leading to additional viscous dissipation. Richard *et al.*[16] argue that in their experiments, bulk of the dissipation is due internal motion inside the drop caused by damped surface oscillations after lift-off. We later quantify such internal dissipation in relation to surface oscillations as a function of Weber and Reynolds numbers. Pasandideh-Fard *et al.*[20] developed a simple model for the maximum extension diameter of the drop, $D_{\max}$, assuming that all the initial kinetic and surface energy is converted to surface energy and viscous dissipation when the drop spreads to its maximum extent. Their model improves upon an earlier model by Chandra & Avedisian[21] which overestimated the value of $D_{\max}$. Clanet *et al.*[22] performed experiments with a low-viscosity drop impacting a superhydrophobic surface for moderate values of Weber number ($2 < We < 900$) where $We = \rho_l V_0^2 R_0/\sigma$ is the Weber number associated with impact velocity $V_0 (= \sqrt{2gH_0})$ for drop of radius R_0 with density and surface tension denoted by ρ_l and σ respec-

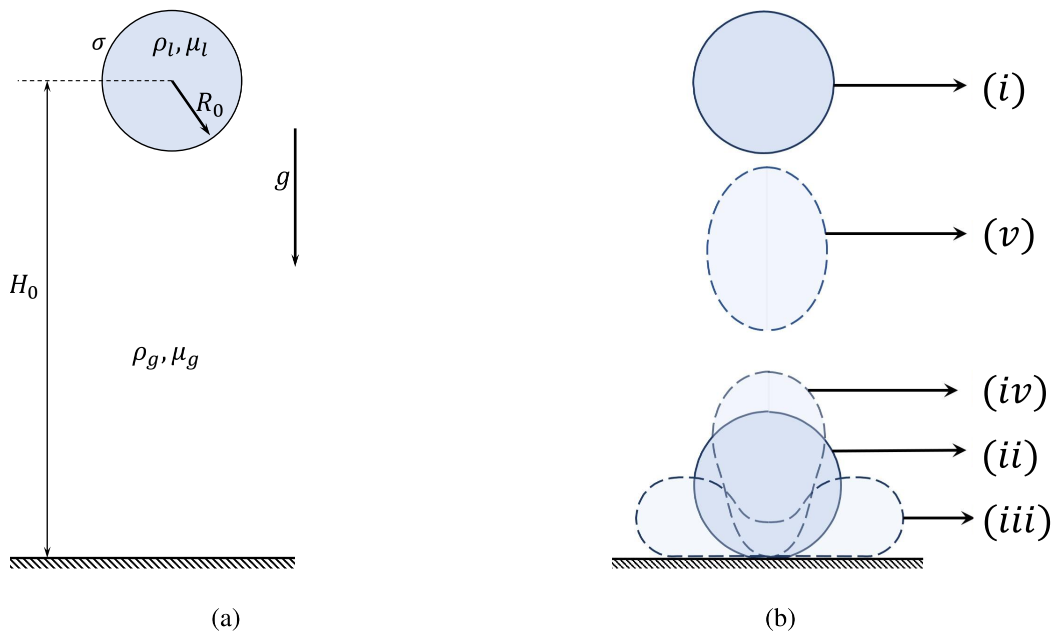

FIG. 1. (a) Schematic of the problem set-up showing all the relevant parameters in the problem. (b) Schematic view of the typical shapes assumed by the drop during one complete bouncing cycle. The solid curves (i, ii) show the shape of the drop at $t = 0$ and at the onset of impact. The other shapes shown with dashed lines at (iii), (iv) and (v) correspond to shape at maximum deformation on the surface, at the instant of lift-off from the surface and at the maximum height after impact, respectively.

tively, and showed that $D_{max} \sim We^{1/4}$. This differs from the low Weber number experiments for drops on superhydrophobic surfaces where a different scaling is observed, $D_{max} \sim We^{1/2}$.

In this study, we use direct numerical simulations to calculate the energy budget of an impacting drop with emphasis on how various exchanges of energies differ as a function of Weber and Reynolds numbers. We further show how coefficient of restitution varies with We and Re which will help resolve the discrepancy between the values reported by de Ruiter *et al.*[11] and Kolinski *et al.*[10].

II. NUMERICAL SET-UP AND ENERGETICS

We numerically simulate a falling drop using the open source code *Gerris* in an axisymmetric configuration. The code, developed by Popinet[23] uses an advanced quatree adaptive mesh refinement and is well know for its accurate interface capture algorithm and surface tension implementation[24]. The geometry used in the current study is identical to a recently completed study for drop impact on solid surface[13]. For suitability of the solver to drop impact dynamics and validation studies, the reader is referred to our companion paper[13].

A drop of radius R_0 is released from an initial height H_0 and a schematic of the problem set-up is shown figure 1. The viscosity ratio between the drop and the surrounding gas is fixed at $\mu_l/\mu_g = 55.5$ mimicking a water drop falling in air. For numerical stability, we keep the density ratio fixed at $\rho_l/\rho_g = 100$ though a value of 1000 showed no appreciable difference in the results. Further, since the focus will be on collision dynamics near the solid surface, viscosity ratio plays a more important role than density ratio. To facilitate complete rebound, the contact angle is kept fixed at 170° inspired by the experiments of Richard & Quéré[14]. For low We and Re, drop bounces without ever making contact with the solid surface. In such cases, the impact is cushioned by a thin film of gas beneath the drop and is referred to as wettability-independent bouncing. In Sharma & Dixit[13], we show that the drop shapes as well as the drop-gas interface profiles during contact are in good agreement with experiments for water in air scenario. Moreover, the numerical results were found to be in excellent agreement with well established scaling laws for the height of the drop when it undergoes its first deformation before impact, $H_d \sim Ca_g^{1/2}$ derived by Pack *et al.*[25], and the minimum thickness of gas film, $h_{min} \sim St^{-8/9}We^{-2/3}$ derived by Mandre *et al.*[7] where $St = \rho_l V_0 R_0/\mu_g$ is the Stokes number. A phase-diagram in the $We-Re$ plane, shown in figure 2, shows two distinct regimes of impact referred to as wettability-independent (WI) contact and wettability-dependent (WD) contact. In the WI regime, the drop is supported on a thin gas layer whose thickness scales with We and St. In the WD regime, contact occurs either at the outer periphery of the drop or near the axis of symmetry. To enable complete rebound, all our simulations are carried out at a fixed contact angle of 170° representing bouncing from superhydrophobic surfaces similar to the experiments of Richard & Quere[14].

The primarily goal of this study is to obtained detailed energy budget as the drop completes one bouncing cycle, i.e., drop from an initial release height H_0 impacts the surface and reaches a new height after lift-off, H_1. During this motion, potential energy of the drop, $E_P(t)$, converts to kinetic and surface energies, $E_K(t)$ and $E_S(t)$. Drag due to surrounding gas as well as internal motions within the drop contributes to viscous dissipation. Let E_0 be the initial energy of the drop given by $E_0 = E_P^{(0)} + E_S^{(0)}$. Applying the principle of energy conservation, the drop has to obey the following relation:

$$E_P(t) + E_K(t) + E_S(t) + D(t) = E_0, \tag{1}$$

where $D(t)$ represents viscous dissipation of energy. It is instructive to combine energies associ-

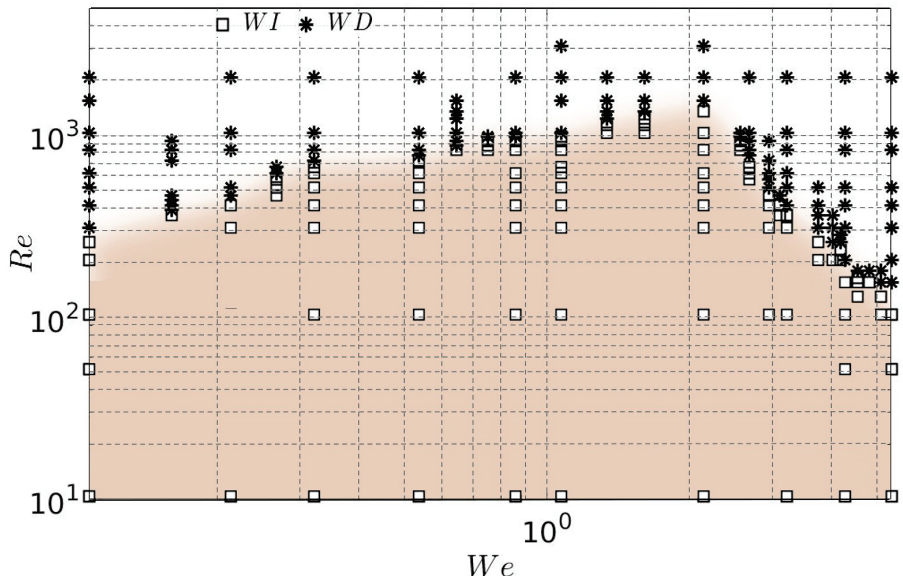

FIG. 2. Phase-diagram in the $Re - We$ plane showing two distinct regimes, the wettability-independent regime (WI) (also shown with a shaded region) and the wettability-dependent regime (WD). The symbols correspond to parameter values where simulations are carried out for one complete bouncing cycle. The transition between the two regimes is grid dependent (see companion paper[13] for more details).

ated only with the drop to highlight the role played by the gas. We therefore define

$$E(t) = E_P(t) + E_{K,d}(t) + E_S(t), \tag{2}$$

where the subscript d in the kinetic energy shows that this energy is only associated with the drop motion. All the energies defined above can be calculated in terms of the flow fields and drop shape numerically using the integrals

$$E_P(t) = \int_\Omega \rho_l B\, g\, h\, d\Omega, \tag{3}$$

$$E_{K,d}(t) = \frac{1}{2}\int_{\Omega_d} \rho_l\,(u^2+v^2)\,d\Omega = \frac{1}{2}\int_\Omega \rho_l B\,(u^2+v^2)\,d\Omega, \tag{4}$$

$$E_{K,g}(t) = \frac{1}{2}\int_{\Omega_g} \rho_g\,(u^2+v^2)\,d\Omega = \frac{1}{2}\int_\Omega \rho_g\,(1-B)\,(u^2+v^2)\,d\Omega. \tag{5}$$

In the above expressions, u and v are radial and axial velocities and B is the volume fraction of liquid with $B = 1$ representing the liquid phase and $B = 0$ representing the gas phase. In the volume-of-fluid method adopted in the current study, the interface cells have a value of B between 0 and 1 such that density of any cell is given by $\rho = B\rho_l + (1-B)\rho_g$. When the drop is not in contact with the solid surface, surface energy is simply the product of surface tension (liquid-gas free energy, σ) and surface area of the drop. But when the drop is in contact with the solid, additional interfacial energy between the drop and the solid, σ_{sl}, needs to be taken into account. For a contact angle, $\theta = \theta_e$, and using Young's law, the surface energy can be defined as,

$$E_S(t) = \begin{cases} \sigma A_s(t) & \text{during flight,} \\ \sigma \left(A_s(t) - a_s(t)\cos(\theta_e)\right) & \text{during contact,} \end{cases} \tag{6}$$

where σ is the surface tension of the drop-gas interface, $A_s(t)$ is the surface area of the drop-gas interface and $a_s(t)$ is the surface area of the drop-solid interface.

Energy lost through viscous dissipation in equn. (1) is obtained by integrating the rate of dissipation of mechanical energy, per unit mass of the fluid, due to viscosity, Φ, as

$$D(t) = \int_0^t \Phi(s)\, ds, \tag{7}$$

where $\Phi(t)$ can be written in terms of the stress tensor $\mathbf{T}$ and rate-of-strain tensor $\mathbf{S}$ as

$$\begin{aligned} \Phi &= \int_{\Omega_d \cup \Omega_g} \mathbf{T} : \mathbf{S}\, d\Omega, \\ &= \int_{\Omega} \left[2\mu \left(\left(\frac{\partial u}{\partial r}\right)^2 + \left(\frac{\partial v}{\partial y}\right)^2 + \left(\frac{u}{r}\right)^2 \right) + \mu \left(\frac{\partial v}{\partial r} + \frac{\partial u}{\partial y} \right)^2 \right] d\Omega. \end{aligned} \tag{8}$$

Here Ω_d and Ω_g representing the drop and gas phases, respectively, and $\mu = B\mu_l + (1-B)\mu_g$ is average viscosity in a cell. Since some of the drop's energy is lost to the kinetic energy of the gas, $E_{K,g}$, we define two new energy terms:

$$E_D(t) = E(t) + D(t), \tag{9}$$

$$E_T(t) = E_D(t) + E_{K,g}(t). \tag{10}$$

The first expression, $E_D(t)$, represents total energy of the drop including viscous dissipation (in drop and gas) while the second expression, $E_T(t)$ is the total energy of the system accounting for all losses, thus E_T should be equal to E_0 at all times. Apart from minor numerical errors, E_T is practically indistinguishable from E_0 in our simulations guaranteeing the numerical accuracy of the solver.

Having defined all the relevant energy quantities, we define two new quantities to quantify energy loss during drop impact. The total energy loss during one complete bouncing cycle, for a

TABLE I. Glossary of important parameters used in the study

Initial energy of the drop ($t=0$)	$E_0 = E_P(t)+E_K(t)+E_S(t)+D(t)$	Equn. (1)
Total energy of the drop	$E(t) = E_P(t)+E_{K,d}(t)+E_S(t)$	Equn. (2)
Potential energy of the drop	$E_P(t)$	Equn.(3)
Kinetic energy of the drop	$E_{K,d}(t)$	Equn.(4)
Kinetic energy of the gas	$E_{K,g}(t)$	Equn.(5)
Surface energy of drop-gas interface	$E_S(t)$	Equn.(6)
Viscous dissipation	$D(t)$	Equn. (7)
Total energy loss	$L_T(t)$	Equn. (11)
Energy loss in contact	$L_c(t)$	Equn. (12)
Coefficient of restitution	$r_c = \sqrt{\lvert V_1\rvert/\lvert V_0\rvert}$	Equn. (14)
Reynolds number	Re	$\frac{\rho_l V_0 R_0}{\mu_l}$
Stokes number	St	$\frac{\rho_l V_0 R_0}{\mu_g}$
Weber number	We	$\frac{\rho_l V_0^2 R_0}{\sigma}$

drop starting at height H_0 till it again attains a new maximum height H_1 after its first impact can be calculated in terms of the total loss, L_T, defined by

$$L_T = E_0 - E_1. \tag{11}$$

Similarly, loss of energy during impact can be calculated as

$$L_c = E_b - E_a \tag{12}$$

E_b and E_a are the total energies of the drop before (taken to be the instant of time at when the drop undergoes its first deformation) and after impact, respectively. Table I summarizes all the energies and parameters used in this work.

III. RESULTS AND DISCUSSION

A. Energy budget

All energies are non-dimensionalized by the initial total energy, E_0, and their variation with time is shown in figure 3 as the drop completes one complete rebound cycle for $We = 3.21$ and

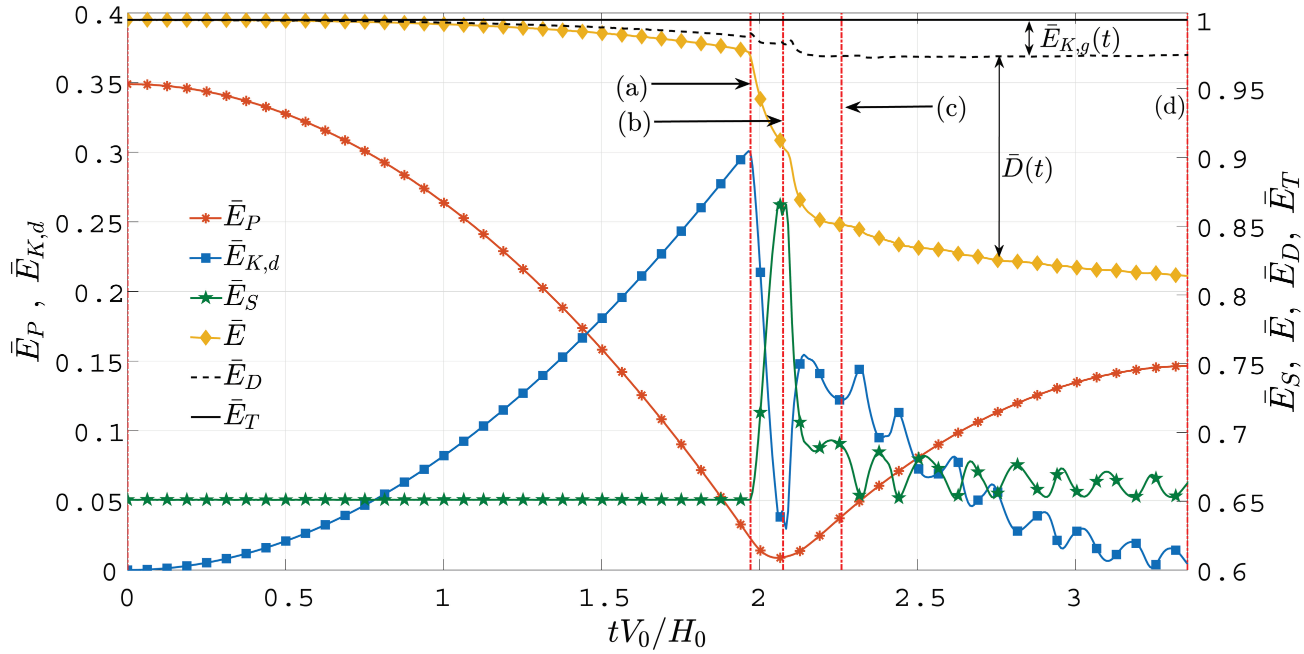

FIG. 3. Energy budget for one complete bouncing cycle for $We = 3.21$ and $Re = 207$ showing various energies associated with the drop and the gas non-dimensionalized with the initial energy E_0. The kinetic, $\bar{E}_{K,d}$, and potential energies, $\bar{E}_P$, are shown on the left y-axis while surface energy, $\bar{E}_S$, energy of the drop without viscous dissipation, $\bar{E}$, energy of the drop with viscous dissipation, $\bar{E}_D$, and total energy of the drop and gas, $\bar{E}_T$, are shown on the right y-axis. See text for more details. Note the difference in scale on both the y-axis. The vertical dash-dot lines shown with (a), (b), (c) and (d) represents time at the onset of impact, at maximum deformation of the drop, at the onset of lift-off and at maximum height, respectively.

$Re = 207$, a case in the wettability independent regime of figure 2. Variations in energy budget is punctuated by distinct phases in drop's evolution during the impact process which are shown by vertical lines marked (a) through (d). The corresponding drop shapes at each of these times is shown in figure 4. At $t = 0$, drop descends from rest possessing only potential and surface energy. The ratio of these two energies is given by

$$\frac{E_P^{(0)}}{E_S^{(0)}} = \frac{We}{6}. \tag{13}$$

In this particular case, $E_S^{(0)} > E_P^{(0)}$ due to the small Weber number used. At the instant shown by (a) in figure 3, drop begins to deform from its spherical shape indicated by a concomitant increase in surface energy. At this instant of time, the kinetic energy of the drop is at its maximum and the drop shape is shown in figure 4(a). A region of high pressure is developed beneath the drop which rapidly decelerates the drop's motion. The drop soon makes 'touchdown', but in this case, supported on a thin cushion of gas below it. The kinetic energy of the drop then rapidly reduces at the expense of its surface energy and the drop deforms to its maximum radial extent at time shown by (b). The drop shape along with the pressure field inside it at this time is shown in figure 4(b). Even at the drop's maximum extent, internal circulation does not completely cease giving rise to a non-zero kinetic energy. In Sharma & Dixit[13], we show that maximum spreading diameter obeys the scaling, $D_{max} \sim We^{1/2}$. This scaling was first derived by Richard & Quéré[14] using the argument of exchange of kinetic and surface energy during impact and the results in figure 3 are consistent with their findings. Surface tension then causes the drop to retract and it eventually achieves lift-off from the solid surface at time (c). The drop takes the shape of a distorted prolate spheroid as shown in figure 4(c). Most of the viscous dissipation occurs during impact as evident from a large decrease in drop's energy, $E(t)$, given in equn. (2), between times (a) and (c). The drop continues to oscillate during its ballistic motion causing additional viscous dissipation due to internal circulation inside the drop. As a result, both kinetic and surface energy exhibit damped oscillations providing a route for continuous loss of drop's energy during its flight. In section IV, we return to the issue of energy loss and compare loss during contact and during flight in greater detail. It has to be noted that only a small fraction of the drop's energy is exchanged with the gas, shown as $E_{K,g}$, in this case, less than 2.5%. During drop's upward motion, we observe a nearly perfect exchange of kinetic and surface energies as shown in figure 5. To compare these energies, we plot only the fluctuating part of the energies obtained by subtracting out the moving-average value. The drop eventually reaches a new maxima, H_1, losing approximately 20% of its total energy E_0, and the drop shape at the new height is shown in figure 4(d).

We now examine how energy budget for a falling drop changes with time for a sample case in the wettability-dependent regime of the phase diagram 2. The energy budget with $We = 3.21$ and $Re = 1035$ is shown in figure 6 and has to be viewed in conjunction with evolution of drop shapes shown in figure 7 as well as three-dimensional and streamline plots showing bubble capture and escape shown in figures 8, 9 and 10 respectively. The evolution of all energies until the first deformation of the drop, shown with vertical dash-dot line at (a), is identical to the previous case at $Re = 207$. Inertia causes the drop to rapidly spread on the surface until time (b) when surface energy reaches a maximum at the expense of kinetic energy. The interface at the axis of symmetry continues to move downwards while the drop retreats inward radially. Capillary waves generated

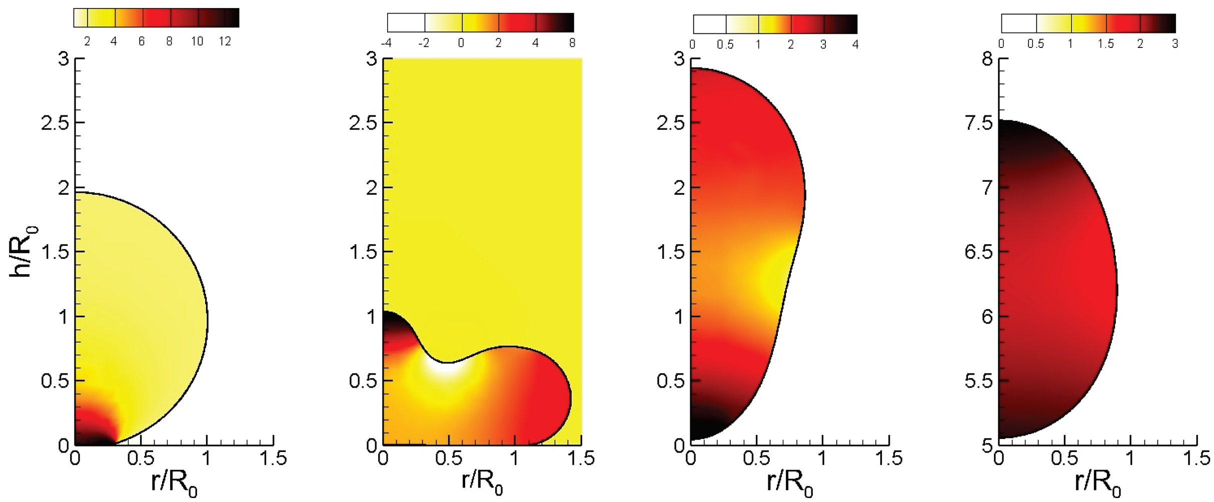

(a) (b) (c) (d)

FIG. 4. Drop shapes for $We = 3.21$ and $Re = 207$ at four different times: (a) $\bar{t} = 1.9719$, (b) $\bar{t} = 2.075$, (c) $\bar{t} = 2.26$ and (d) $\bar{t} = 3.349$. The colour contours show the variation of non-dimensional pressure, $\bar{P} = P/(\sigma/R_0)$. The four panels corresponding to time instants shown with vertical dash-dot lines in the energy budget 3. Note that contour levels are different in the four panels.

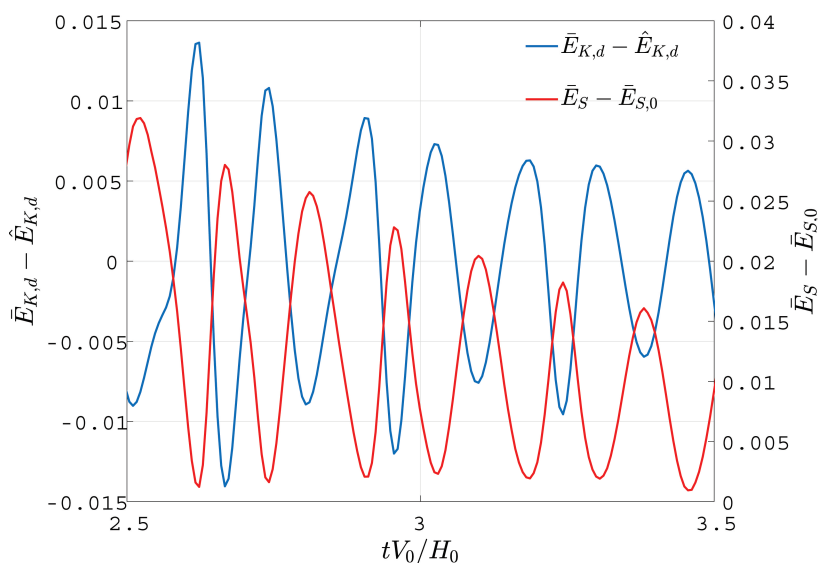

FIG. 5. A close-up view of the fluctuating part of the kinetic and surface energies of the drop after rebound, from figure 3, showing perfect exchange of energies between the two. $\hat{E}_{K,d}$ represents the moving-average value of the kinetic energy and $\bar{E}_{S,0}$ is initial surface energy of the drop.

near the surface travel azimuthally along the drop's surface amplifying in the process. These waves focus at the axis of symmetry resulting in vigorous vertical oscillations of the upper interface of

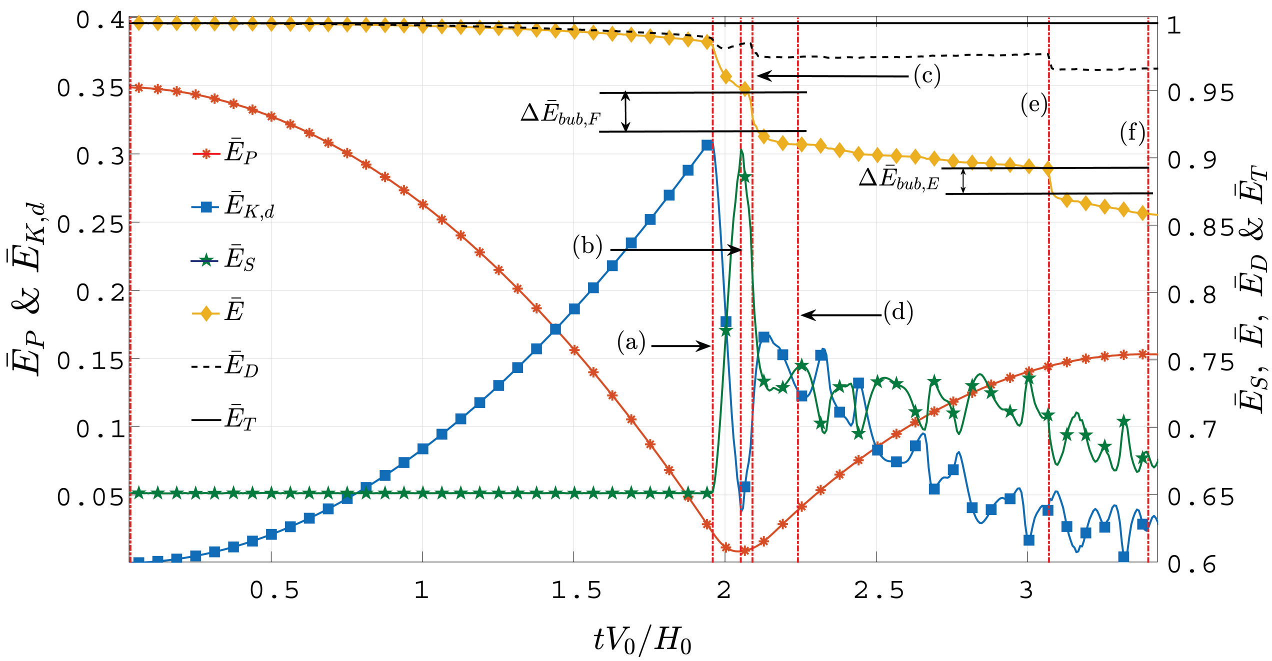

FIG. 6. Energy budget for one complete bouncing cycle for $We = 3.21$ and $Re = 1035$ showing various energies associated with the drop and the gas non-dimensionalized with the initial energy E_0. All quantities are the same as defined in figure 3. The vertical dash-dot lines shown with (a), (b), (c), (d), (e) and (f) represents times at the onset of impact, at maximum deformation of the drop, at the instant of bubble entrapment, at the onset of lift-off, at bubble escape and at maximum height after impact, respectively.

the drop as shown in figure 8(a). The interface then descends downwards and undergoes necking. This process traps a gas bubble inside it as shown in 8(d). Cusp-like regions are formed at the axis of symmetry which results in localised regions of high pressure, figure 7(c). Fluid rapidly moves away from this high pressure zones resulting in the formation of a high speed jet. On the upper side, the high speed jet breaks up into tiny drops due to rapid acceleration, whereas on the lower side, this jet can collide with the trapped bubble generating tiny secondary bubbles inside the bubble (see supplementary movie-1). The intense motion results in some of the drop's energy to be lost to accelerate the gas, some to viscous dissipation due to rapid and vigorous motions inside the drop and a small portion to mass lost from ejection of tiny droplets. This process occurs over a very short timescale, shown at time (c), and causes a sudden drop in the drop's energy, shown as $\Delta\bar{E}_{bub,F}$, which represents the energy lost during bubble entrapment. We show later that bubble entrapment and escape result in a sudden increase in viscous dissipation. Figure 9 shows the sequence of events leading to trapping of the bubble. Large scale inward motion of the drop as shown in figures 9(a)-(c) shows trapping of a gas bubble inside the drop. Strong vortical flow is generated inside bubble as revealed in close-up views shown in figures 9(e)-(f) consistent with the findings of Tripathi *et al.*[26] who noted that vorticity tends to concentrate in the lighter fluid. At the end of the bubble entrapment process, the upper interface of the drop tends to violently recoil releasing a high speed jet. Contours of velocity magnitude in figure 9 reveals that significantly high velocities are generated in the gas phase, particularly after the complete enclosure of the bubble inside the drop. In physical terms, consider a $1mm$ water drop impacting a surface with the same We as given in figure 9. This translates to impact speed, $V_0 \approx 0.46m/s$ which leads to gas velocity of about $46m/s$.

The trapped bubble remains lodged inside the drop during lift-off at time (d) in figure 6 and also shown in figure 7(d) and in some cases even stays inside the drop until drop undergoes its second bounce. In this particular case, the trapped bubble slowly drifts upwards and eventually emerges out of the drop in a violent escape at time (e). During its emergence, the bubble traps a thin curved film of liquid between its upper surface and the drop's surface. This thin film ruptures at its periphery as shown in figure 7(e) similar to the process described in Manica *et al.*[27]. Very large pressures are generated at the tip of the filament due to tiny curvatures there (see inset of figure 7(e)). This causes the tip to rapidly retract allowing pressurised gas inside the bubble to rapidly escape imparting kinetic energy to the gas. Figure 10 shows bubble escape process in finer detail. A thin film of liquid is trapped between the upper surface of the drop and the escaping bubble as shown in figure 10a. As soon as the rupture is initiated, pressurised gas inside the bubble rapidly escapes as evident from the contours of velocity magnitude shown in figure 10(b,c). Simultaneously, the thin liquid film shown in 10d, now in the form of a filament, rapidly retreats radially in a time of approximately $\Delta\bar{t} \approx 8 \times 10^{-4}$. In dimensional terms, this amounts to a time of about 30 μs. A counter-rotating toroidal vortex pair, figure 10e, is generated in the gas generating a great deal of viscous dissipation. The retracting filament collapses upon itself resulting in a vertically accelerating jet (figure 10f) which can hit the drop during its rebound and entrap tiny gas bubbles again. These tiny secondary bubbles as seen in figure 7(f) may again create tertiary bubbles, but our simulations do not have sufficient resolution to track escape of these bubbles. See supplementary movie - 2 to see a 3D visualization of an escaping bubble. The process of bubble escape causes a sudden drop in the drop's total energy, $\Delta E_{bub,E}$ as shown at time (e) in figure 6 where the subscript E denotes an escaping bubble.

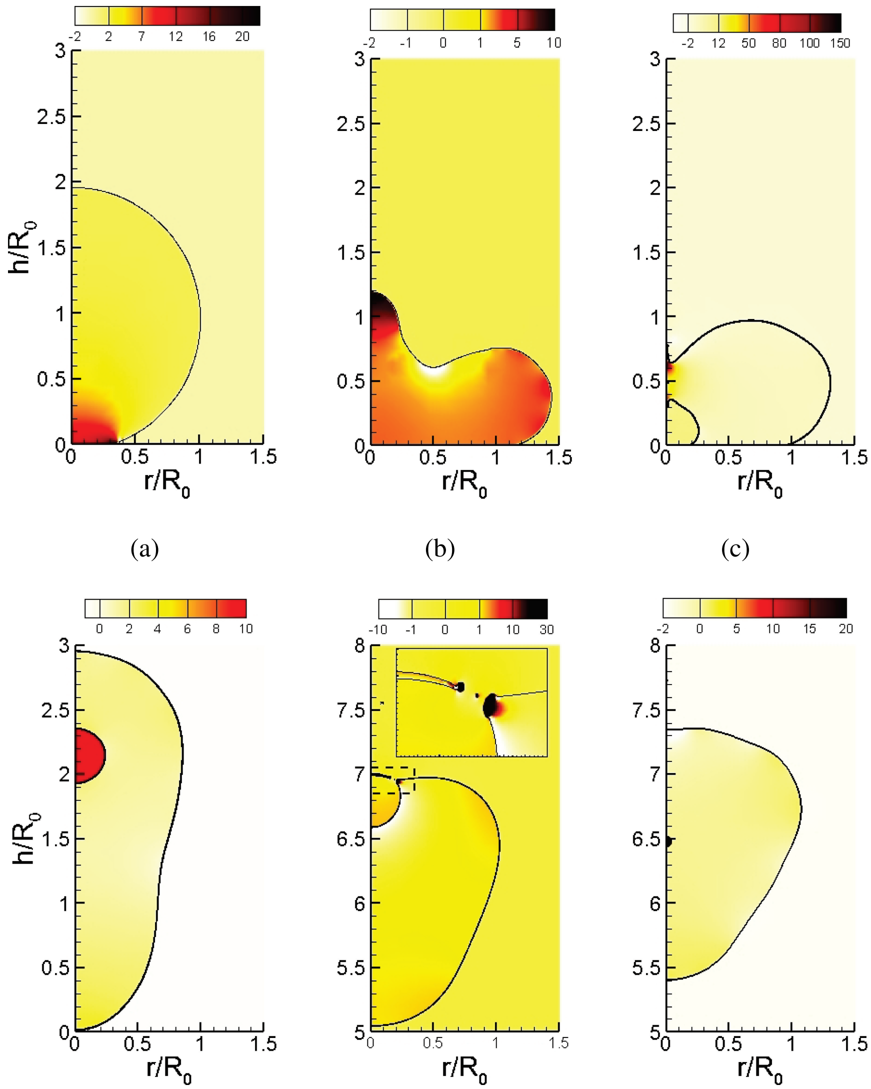

(a) (b) (c)

(d) (e) (f)

FIG. 7. Drop shapes for $We = 3.21$ and $Re = 1035$ at six different times: (a) $\bar{t} = 1.959$, (b) $\bar{t} = 2.047$, (c) $\bar{t} = 2.09$, (d) $\bar{t} = 2.241$, (e) $\bar{t} = 3.071$ and (f) $\bar{t} = 3.374$. The colour contours show the variation of non-dimensional pressure, $\bar{P} = P/(\sigma/R_0)$. The six panels corresponding to time instants shown with vertical dash-dot lines in the energy budget 6. Note that contour levels are different across the panels. See supplementary online material showing a three-dimensional evolution of bubble entrapment and escape.

B. Coefficient of restitution

In the above discussion, energy budgets were presented for two specific parameter values, viz., $Re = 207, We = 3.21$ and $Re = 1035, We = 3.21$. A number of interesting facts emerged from this analysis which are briefly listed below: (i) energy loss occurs when the drop is in contact with the

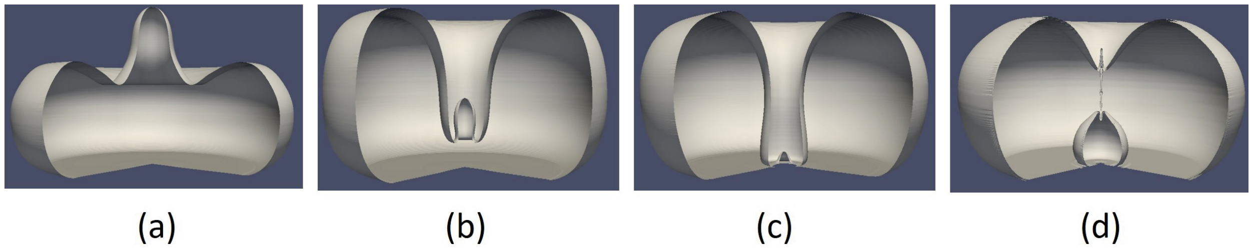

FIG. 8. Three-dimensional representation of drop shapes showing the process of bubble entrapment during drop impact. The four panels are in sequence (from left to right) at non-dimensional time $\hat{t} = (t - t_0)/\tau$: (a) 0.82 at maximum spreading, (b) 1.01, at intermediate stage of downward motion of upper interface, (c) 1.06 at the onset of necking of the cylindrical filament, and (d) 1.12, high speed jet ejection at the axis of symmetry, where t_0 is time of first deformation. Parameters used are $We = 3.21$ and $Re = 1035$. See supplementary online material showing a three-dimensional evolution of bubble entrapment.

solid surface, (ii) energy loss occurs when the drop is in motion after bouncing from the surface. The former occurs primarily due to large shear stresses generated near the solid surface, both in the gas and the drop, while the latter occurs due to surface oscillations-induced internal motions inside the drop which generates additional viscous dissipation. We estimate both these energy losses for the entire range of We and Re shown in the phase diagram 2. Conventionally, energy loss during impact is represented through the coefficient of restitution defined as

$$r_c = \frac{|V_1|}{|V_0|}, \tag{14}$$

where V_1 is the velocity after impact and V_0 is the velocity of the drop before impact. In the case of a drop which is undergoing large shape changes, velocity is often difficult to determine in experiments. In such cases, a height-based coefficient of restitution has sometimes been used:

$$r_h = \sqrt{\frac{H_1}{H_0}}, \tag{15}$$

where H_1 is the maximum height attained by the drop after the impact and H_0 is the initial release height at $t = 0$.

The two definitions of restitution coefficient will be the same if viscous dissipation in the drop during its ballistic motion before and after impact as well as drag from the surrounding gas is negligible.

De Ruiter *et al.*[15] reported a coefficient of restitution, $r_c \geq 0.88$ and in some cases, reported values as high as 0.96 ± 0.04. This value is in contrast to the value reported by Kolinski *et al.*[10]

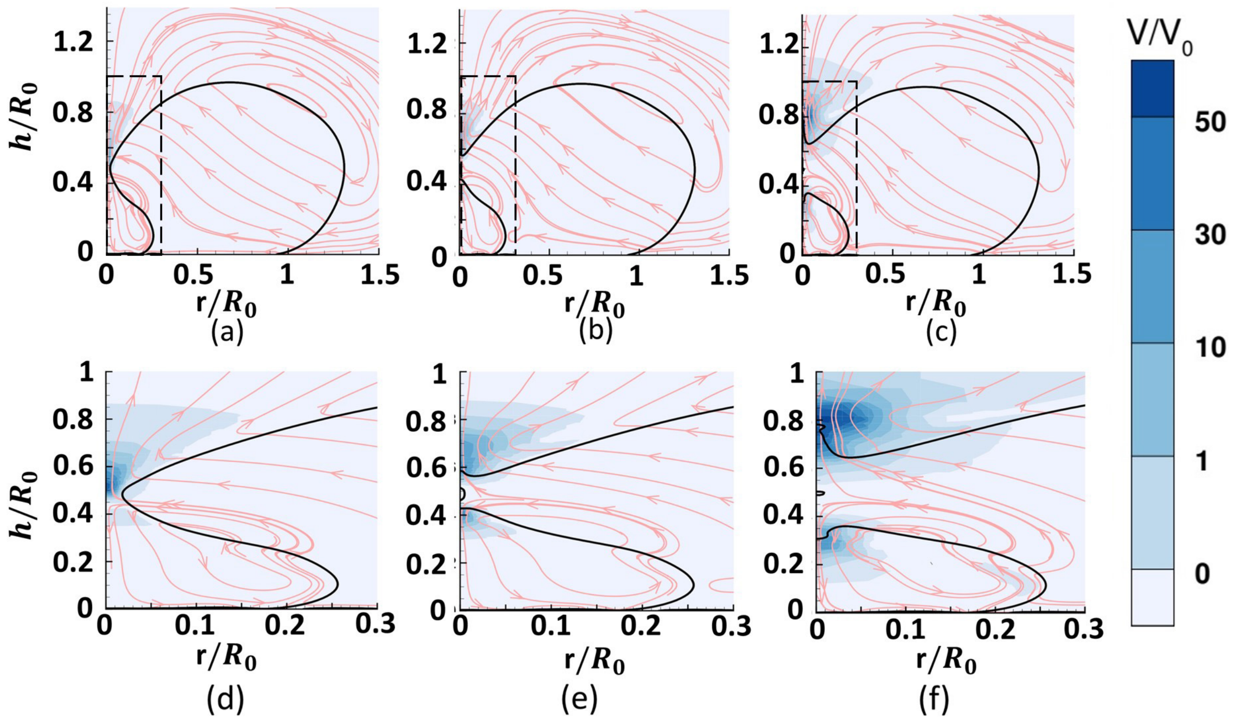

FIG. 9. Flow field during bubble entrapment process for $We = 3.21$ and $Re = 1035$ showing instantaneous streamlines and contours of velocity magnitude at (a) $\bar{t} = 2.0902$, (b) $\bar{t} = 2.0904$, (c) $\bar{t} = 2.0908$. Close-up views shown in panels (d), (e) and (f) shows vortical motion inside the trapped bubble. The high speed jet generates intense velocities near the axis of symmetry imparting kinetic energy to the gas and also causes viscous dissipation during bubble entrapment. See supplementary online material showing a three-dimensional evolution of bubble entrapment.

who reported $r_h \leq 0.65$ based on a height-based measurement and it was suggested that such low values in r_h are due to formation of a strong shear-layer in the gas cushion beneath the drop. De Ruiter *et al.*[15] use water drops in their experiments whereas Kolinski *et al.*[10] use water-glycerol mixtures which increases the viscosity of the drops. Further, the impact velocities are lower in the latter case which results in lower *Re* values. In both the studies, the surfaces are hydrophilic and the drops never make physical contact with the solid surface for the entire range of *Re* and *We* considered in the present study. The large variation in the value of restitution coefficient in the two studies can be reconciled by examining the role of *Re* and *We* in these experiments. High values of r_c were also reported in the works of Foote[28] and Richard & Quéré[14], the former being a numerical study for head-on collision of two drops while the latter is an experimental study of drops bouncing on superhydrophobic surfaces. De Ruiter *et al.*[15] attributed such high values to

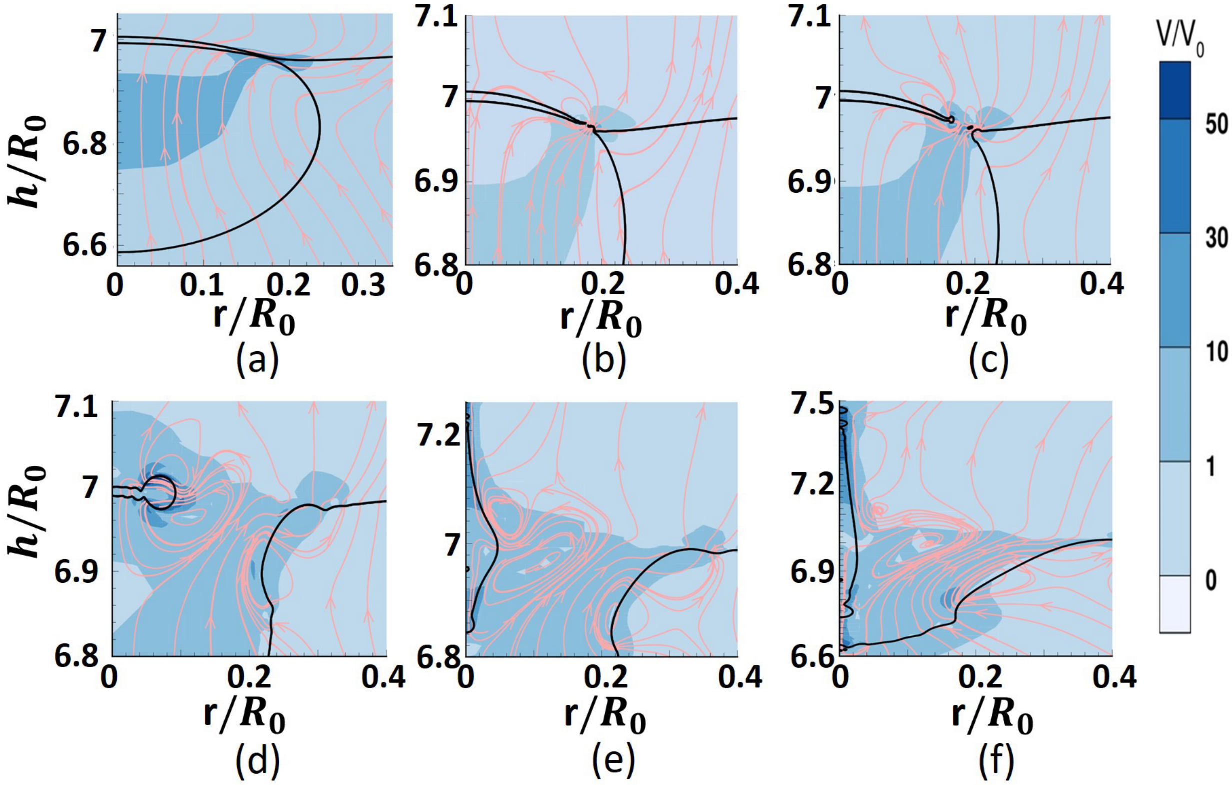

FIG. 10. A close-up view of the fluid motion generated during escape of the entrapped bubble. A thin liquid film trapped between the escaping bubble and the upper surface of the drop ruptures (a,b) and rapidly retreats (c,d). This generates another high speed jet at the axis of symmetry (e,f). The panels are shown in sequence at non-dimensional times, $\bar{t}$: (a) 3.0705, (b) 3.071, (c) 3.0711, (d) 3.0718, (e) 3.0724, (f) 3.0737. See supplementary online material showing a three-dimensional evolution of bubble escape.

the absence of contact line and the strong repulsion force provided by lubricating gas layer while Richard & Quéré[14] attributed high values of r_c to the low contact time in their experiments. It is possible that contact-less bouncing also occurred in Richard & Quéré[14], but there is no evidence of this in their paper. Richard & Quéré[14] suggest that a great deal of energy loss occurs when the drop is in flight. By calculating the kinetic energy based on the centre of mass of the drop as well as kinetic energy due to internal motions inside the drop, de Ruiter *et al.*[15] obtained a detailed energy budget of the drop. Major losses during each bounce was attributed to viscous losses in the thin lubricating gas layer. This is consistent with the reason provided by Kolinski *et al.*[10] who attributed low r_c in their experiments to large dissipation in the gas layer.

The above survey suggests that viscous losses in the thin intervening gas layer varies as a

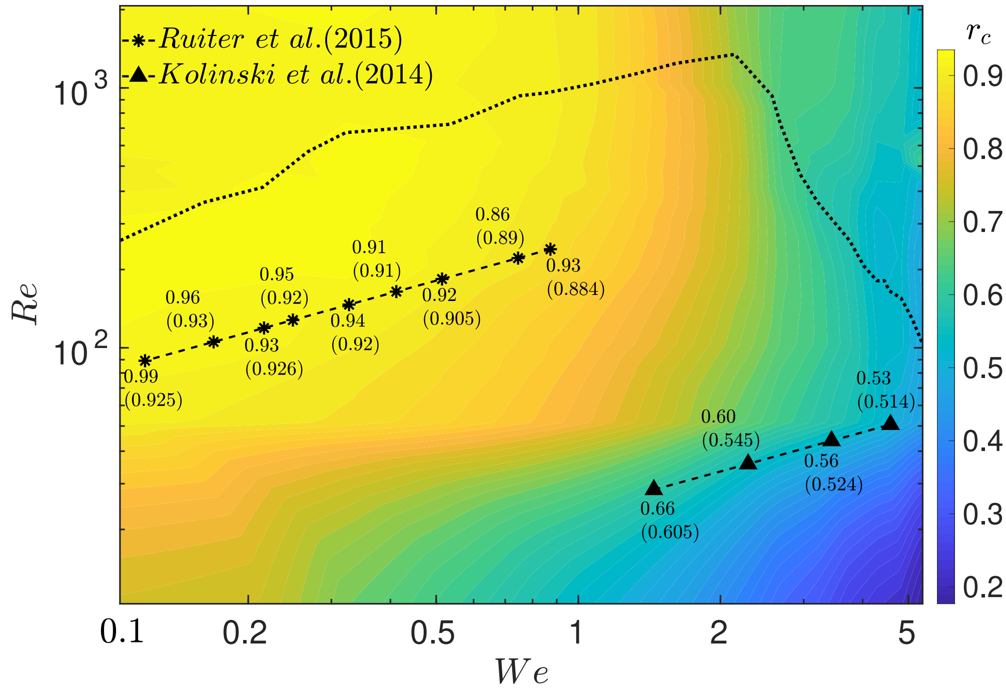

FIG. 11. Variation of coefficient of restitution, r_c, on the $We-Re$ plane. The experimental values obtained by de Ruiter *et al.*[15] (water droplet impact on glass) and Kolinski *et al.*[10] (water-glycerol drop on mica) are shown along with simulation shown in brackets. Simulation values are within 10% of the experimentally obtained values.

function of St and We, where $St = Re/\lambda$ is the Stokes number and $\lambda = \mu_g/\mu_l$ is the viscosity ratio. To reconcile differences between the above studies, we extract the coefficient of restitution r_c from our simulation data and plot it in the $We-Re$ plane as shown in figure 11. The experimental values of restitution coefficient in de Ruiter *et al.*[15] and Kolinski *et al.*[10] are shown with symbols while the simulation values at the same Re and We are shown alongside in brackets. It is clear that the agreement with simulations and experiments is satisfactory. More importantly, our simulations reveal that restitution coefficient strongly varies with both Re and We. The differences observed in the two sets of experiments can thus be attributed to very different experimental parameters used in the two studies. Figure 11 also reveals that for $We \gtrapprox 1$, r_c becomes less sensitive to Reynolds number and rapidly decreases with increase in We. At higher We, drop undergoes large scale deformation generating a great deal of vigorous motions inside the drop. This motion coupled with lower values of surface tension at higher We causes the drop to spread to greater extent on the solid surface obeying the scaling law $r_k \sim We^{1/4}$ where r_k is the radial extent of the gas layer (see Sharma & Dixit[13]). This generates a strong shear in the gas layer generating excess dissipation

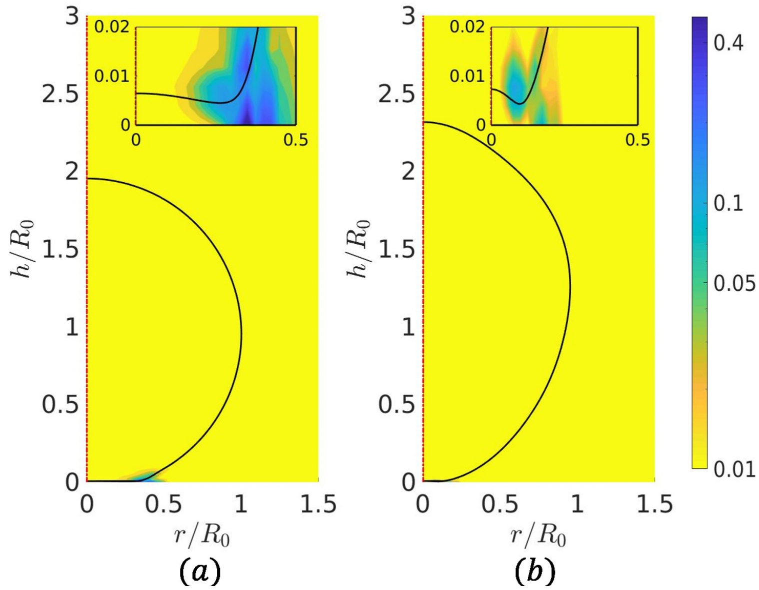

FIG. 12. Contours of non-dimensional rate of dissipation (Φ/Φ^*) during spreading and receding stages of the drop for $We = 1.07$ and $Re = 207$ at (a) $\hat{t} = 0.19$ and (b) $\hat{t} = 2.372$. The inset shows drop-gas interface profile near the solid surface where the rate of dissipation is maximum.

at the location of h_{min}, i.e. where the gas layer is at its thinnest. This can be easily verified by determining non-dimensional rate of dissipation written as Φ/Φ^* where Φ is given by equn. (8) and Φ^* is the characteristic value of dissipation. Using impact velocity V_0 and gas layer thickness when the drop undergoes its first deformation, $H_d \sim R_0 Ca_g^{1/2}$[13], we have $\Phi^* = V_0 \sigma / \lambda R_0^2$. Contours of Φ/Φ^* shown in figure 12 at two different times show that dissipation indeed assumes large values in the thin gas film, both during spreading and receding stages. Low values of dissipation are found inside the drop consistent with the observation in Gopinath & Koch[29] who noted that for $Re \gg We^{1/2}$, viscous dissipation inside the drop can be neglected.

At lower We, figure 11 shows that r_c strongly depends on the value of Re at lower Reynolds numbers and weakly depends on Weber number. This is a direct consequence of increased viscosity at lower Re which causes large dissipation in the gas film. At low We, deformation of the drop is also reduced, thus r_c values remain relatively high in this region for a wide range of Reynolds numbers as seen in figure 11. The role of We and Re becomes even more evident in figure 13 where non-dimensional viscous dissipation, $\bar{D} = D/E_0$ is plotted for four different parameter combinations. This can be explained using the simple analogy of a mass-spring-damper system given by

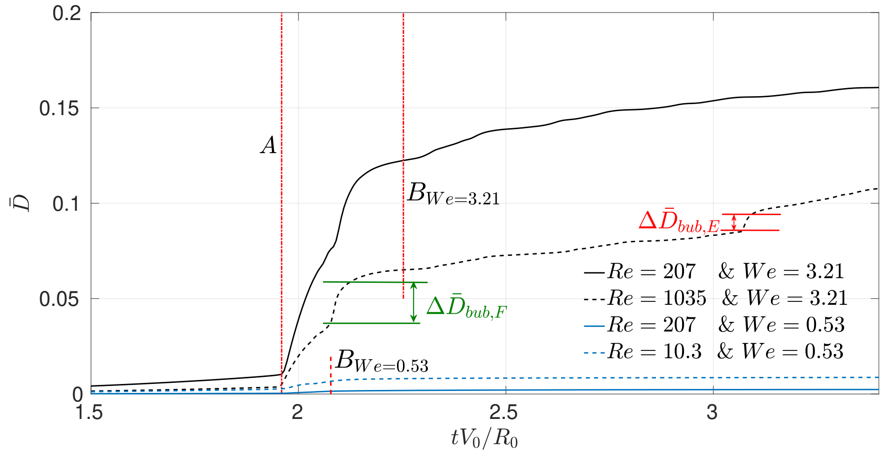

FIG. 13. Variation of non-dimensional viscous dissipation, $\bar{D} = D/E_0$ for four combinations of Re and We. The vertical dash-dot and dashed lines, common for the same value of We, shows the time instant when contact begins (shown as A) and when the drop departs the surface (shown as B).

$$m\ddot{y} + \gamma(We, Re)\dot{y} + k(We)y = F(t), \tag{16}$$

where damping coefficient γ is a function of both Re and We whereas stiffness k is a function of We alone. For very low We, surface tension dominates over inertia and the drop does not exhibit large scale oscillations on its surface. In this limit, the drop largely remains spherical and dissipation/damping simplifies to $\gamma \approx \gamma(Re)$. But at higher We, large scale oscillations inside the drop induces undulations in the underlying gas layer beneath the drop[13]. The radial extent of the gas layer is large at high We which generates strong shear stress in the gas layer causing viscous dissipation. Further, surface oscillations induced motions contributes to additional viscous dissipation during drop motion in flight.

The effect of We and Re or St on viscous dissipation can be understood through a simple scaling law derived below. Viscous dissipation during contact given in equn. (8) scales as

$$D \sim \mu_g \left(\frac{V}{h}\right)^2 \Omega\, T, \tag{17}$$

where V and h are characteristic velocity and length scales in the gas film, Ω is the volume of the gas film beneath the drop and T is the characteristic time scale. Using impact velocity V_0 for velocity, gas thickness at the drop's first deformation, H_d, for thickness and inertia-capillary time

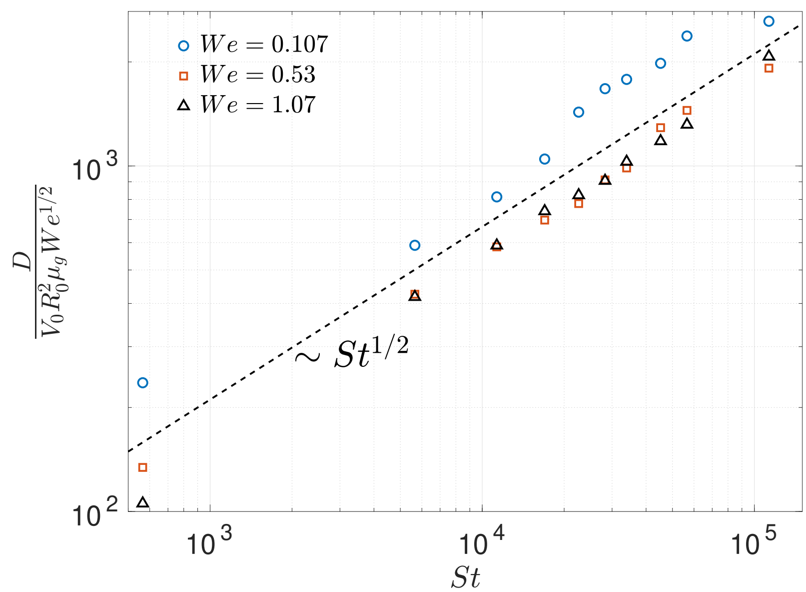

(a)

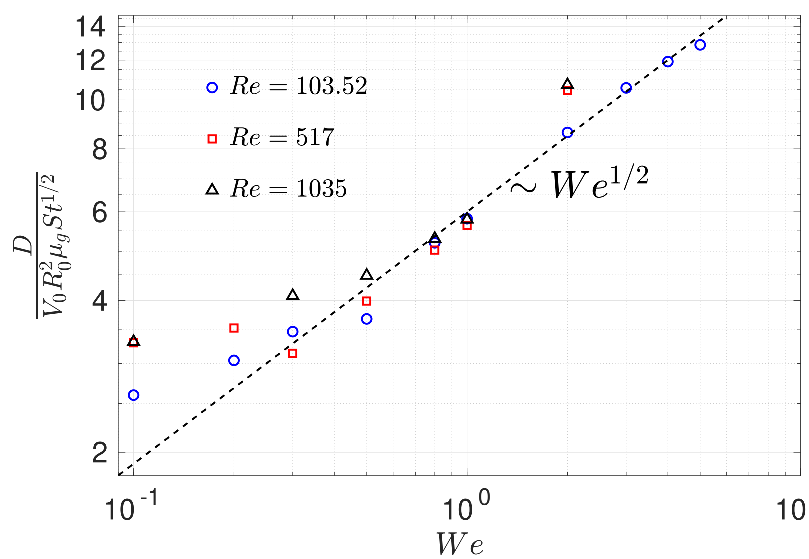

(b)

FIG. 14. Scaling for non-dimensional viscous dissipation as a function of (a) Stokes number, (b) Weber number. The symbols in each plot correspond to three different values of Weber numbers (a) or Reynolds numbers (b). The dashed line shows the scaling law given by equation (19).

scale $\tau \sim (\rho_l R_0^3/\sigma)^{1/2}$ for time, we have

$$\begin{aligned} D &\sim \mu_g \left(\frac{V_0}{H_d}\right)^2 \pi\, r_k^2\, H_d\, \tau, \\ &\sim \mu_g \frac{V_0^2}{H_d} r_k^2 \tau \end{aligned} \tag{18}$$

,

where Ω is taken to be the volume of a uniform gas film of thickness H_d and radius r_k. In Sharma & Dixit[13], we show that $H_d \sim R_0 Ca_g^{1/2}$ where $Ca_g = We/St$ is capillary number based on gas viscosity and $r_k \sim R_0 We^{1/4}$. Using these expressions, viscous dissipation reduces to

$$D \sim \mu_g V_0 R_0^2\, We^{1/2} St^{1/2}. \tag{19}$$

Figure 14(a) and 14(b) shows variation of non-dimensional viscous dissipation with Stokes number (at fixed We) and Weber number (at fixed St) and the agreement with the scaling law derived in equn. (19) is excellent except for low values of We. Our scaling law derivation makes two important assumptions, (i) validity of the lubrication approximation, (ii) time scale $T \approx \tau$. At very low We, the extent of the gas film, defined as the radial location of the outer minima in gas film thickness, follows the scaling $r_k \sim R_0 We^{1/4}$. Hence in the low We cases, lubrication approximation becomes questionable. Following the work of Moláček & Bush[18] who showed that, at low We, time of contact increases with decrease in Weber number, our second assumption becomes questionable at low We. These two reasons explain the deviation of our results in figure 14(b) from the scaling law (19).

IV. ENERGY LOSSES DURING A BOUNCING CYCLE

In the previous section, coefficient of restitution was estimated based on the velocities before and after impact. Richard & Quéré[14] estimated that most of the energy lost in their experiments were due to viscous dissipation during flight. This can occur owing to drag from the surrounding gas and internal motions generated inside the drop due to surface oscillations. It is also relevant to note that Kolinski *et al.*[10] calculate coefficient of restitution based on maximum drop heights given in equn. (15). Large amplitude multi-mode drop oscillations generates large internal circulations inside the drop which leads to viscous dissipation which cannot be accounted for in restitution coefficient based on change in velocity during impact. In figure 15(a), we first plot the total energy loss, $L_T = E_0 - E_1$, that occurs during one complete bouncing cycle, i.e. till the centroid of the drop attains a maxima after impact. The contour of energy loss, L_T, strongly depends on We as evident from the nearly vertical contours. At large We, energy loss reaches to about 0.4, i.e. 40% of drop's energy is lost in one bouncing cycle.

To investigate whether this loss occurs during contact or during flight, we plot the ratio of energy lost during contact to total energy lost, L_c/L_T, as shown in figure 15(b). We are primarily interested in the wettability-independent region which occurs below the dotted curve in 15(b). Consistent with the discussion in the previous section, at high We energy lost during contact is the primary contributor for total energy loss and can be upto 80% of the total loss. At high Weber number, which is also the region of interest in Kolinski *et al.*[10], the drop assumes complex shapes generating a great deal of internal motion inside the drop[13]. This results in significant energy loss during contact. But at very low We where the contact time is also very short, most of the energy is lost during flight. At $We \approx 1$, the loss of energy is nearly equipartitioned between loss during contact and loss during flight. Figure 15(b) is one of key findings of this study and establishes the role of We unequivocally on energetics of drop impacts. The patchy region that occurs in the wettability-dependent region at high Re and We is also the region where bubble entrapment and escape occurs. Energy loss during contact in this region depends on the precise nature of bubble entrapment process which requires further study.

The role of Weber number is best illustrated by examining its effect on the drop shape during impact. We illustrate this with one specific example taken at $Re = 51.7$ and at $We = 2.14, 3.21$. Modal decomposition is carried out by expanding the drop shape in terms of Legendre polynomials:

$$R(t,\theta) = R_0 + \sum_{n=0}^{\infty} c_n(t) P_n(\cos\theta), \tag{20}$$

where n is the mode number, $P_n(\cdot)$ is Legendre polynomial of order n and $c_n(t)$ is the corresponding coefficient. We use the orthogonality of the Legendre polynomials, to estimate c_n in terms of drop shapes:

$$c_n(t) = \frac{2n+1}{2} \int_{-1}^{1} (R(t,\theta) - R_0) P_n(\cos\theta) d(\cos\theta). \tag{21}$$

We extract the coefficients c_n for two different Weber numbers at various times as shown in figure 16 for the first 10 modes. At $We = 0.53$, dominant surface mode of the drop occurs at $n = 2$

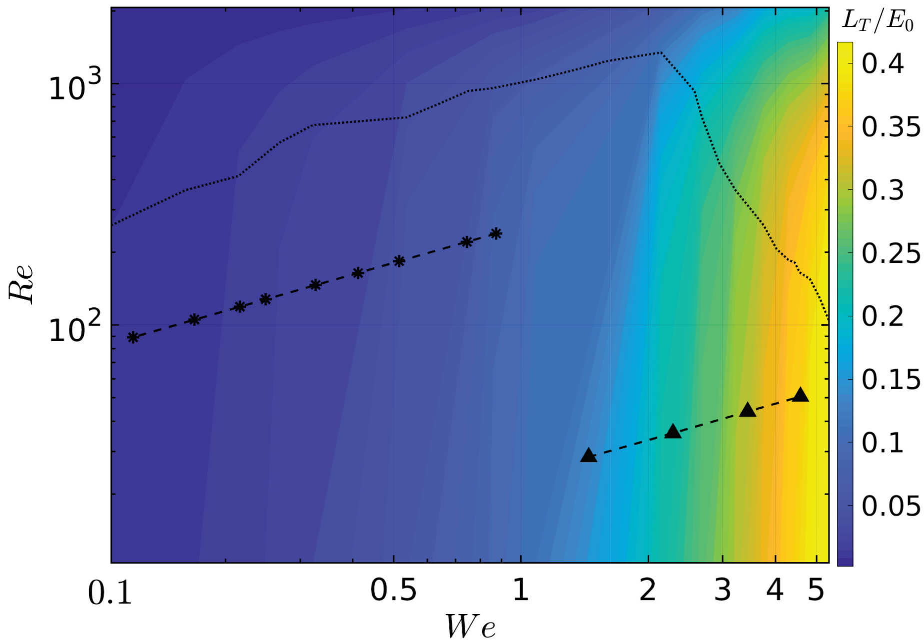

(a)

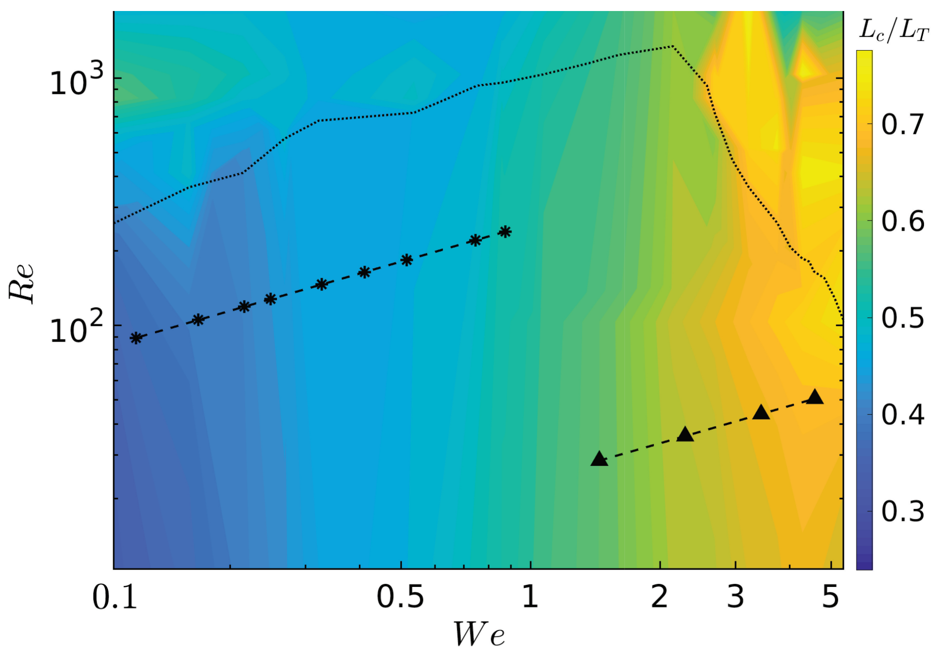

(b)

FIG. 15. Variation of (a) energy loss during one complete bouncing cycle, L_T/E_0 and (b) relative contribution of energy loss during contact vis-à-vis total energy loss, L_c/L_T. Panel (a) shows that maximum energy loss occurs at high Weber numbers and is only weakly dependent on Reynolds number. Panel (b) shows that at higher Weber numbers, contact losses dominate over energy loss that occurs during flight. The symbols correspond to experimental parameters used in de Ruiter *et al.*[15] ($*$) and Kolinski *et al.*[10] (▲).

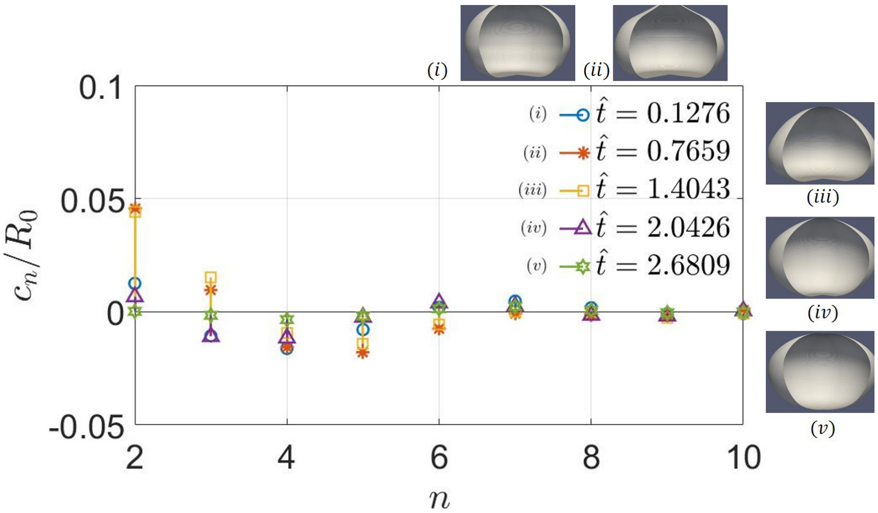

(a)

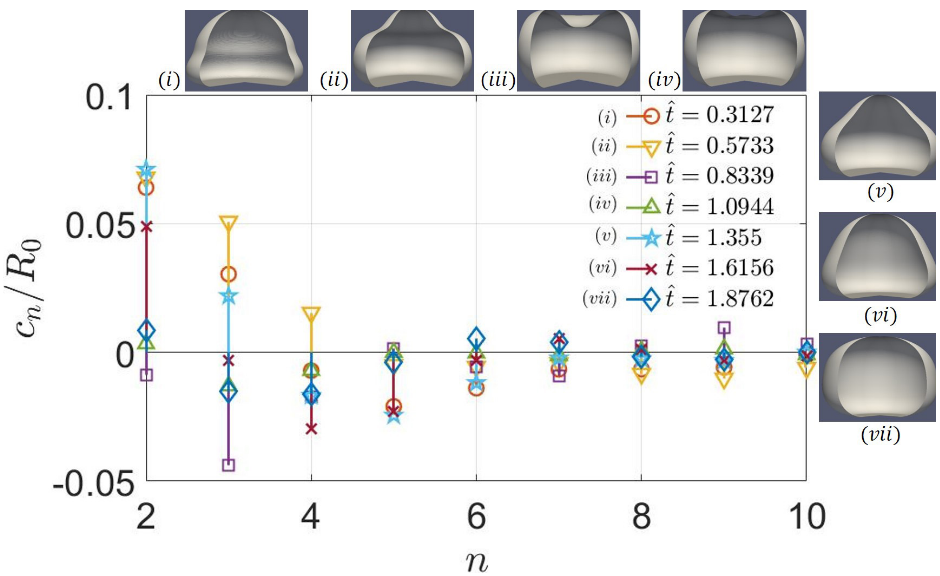

(b)

FIG. 16. Modal decomposition for two different cases: (a) $We = 0.53$, $Re = 51.7$, (b) $We = 3.21$, $Re = 51.7$ at various times during drop evolution. For lower values of Weber numbers, the fundamental oscillation mode $n = 2$ absorbs most of the energy whereas at higher Weber numbers, energy is distributed to higher modes too. Three-dimensional drop shapes shown in each panel correspond to the instants of time when decomposition is carried out.

which corresponds to a prolate-oblate shape transition throughout the contact process while higher modes have a significantly lower amplitude. But at $We = 3.21$, significant energy is transferred to higher modes which also leads to faster decay of energy of the drop at this Weber number.

Propsperetti[30] studied the viscous decay of an oscillating drop and obtained the decay rate of surface oscillations as

$$b_0 = (n-1)(2n+1)\frac{\mu_l}{\rho_l R_0^2}. \tag{22}$$

This is consistent with the expression for viscous dissipation obtained by Moláček & Bush[18] assuming the flow is approximately irrotational inside the drop:

$$D = 8\pi\mu R_0^3 \sum \left(\frac{n-1}{n}\right) c_n^2 \tag{23}$$

As one may expect, higher modes indeed decay more rapidly than lower modes as is also found in our simulations.

V. SUMMARY AND CONCLUSIONS

In the current work, we present an axisymmetric numerical study of drop impacting a dry solid surface. In a related study by Sharma & Dixit[13], it was shown that drop impact dynamics can be divided into a wettability-dependent and wettability-independent regimes depending upon the value of Reynolds and Weber number. The present study explores energetics of drop impact with the aim of investigating role of Reynolds and Weber numbers on the coefficient of restitution. A parametric study is carried out for a wide range of Re and We at fixed density and viscosity ratios. In each case, potential, kinetic and surface energies as well as viscous dissipation is calculated for one complete bouncing cycle. Detailed energy budget is presented for two special cases at $We = 3.21$ and $Re = 207, 1035$ shown in figures 3 and 6. Before impact, surface energy remains constant while gravitational potential energy is converted to kinetic energy. Due to low values of gas viscosity used in the current study (equivalent of an air-water system), viscous dissipation due to drag is negligible. The onset of impact is indicated by a steep rise in surface energy at the expense of the drop's kinetic energy until the drop spreads to its maximum radial extent. In the wettability-independent bouncing process where the drop is supported on a thin cushion of gas, rapid recoil occurs resulting in sharp decline of surface energy. In the wettability-dependent process, recoil occurs only for hydrophobic and superhydrophobic surfaces like in the present study. Even for such impacts, drop first spreads on a thin gas film sometimes referred to a 'skating process'[9] before contact eventually occurs. Strong shear is generated in the gas layer below causing a large amount of viscous dissipation. The drop eventually lifts-off completing the contact process. The energy loss that occurs during contact, L_c, is the major contributor in total loss, L_T,

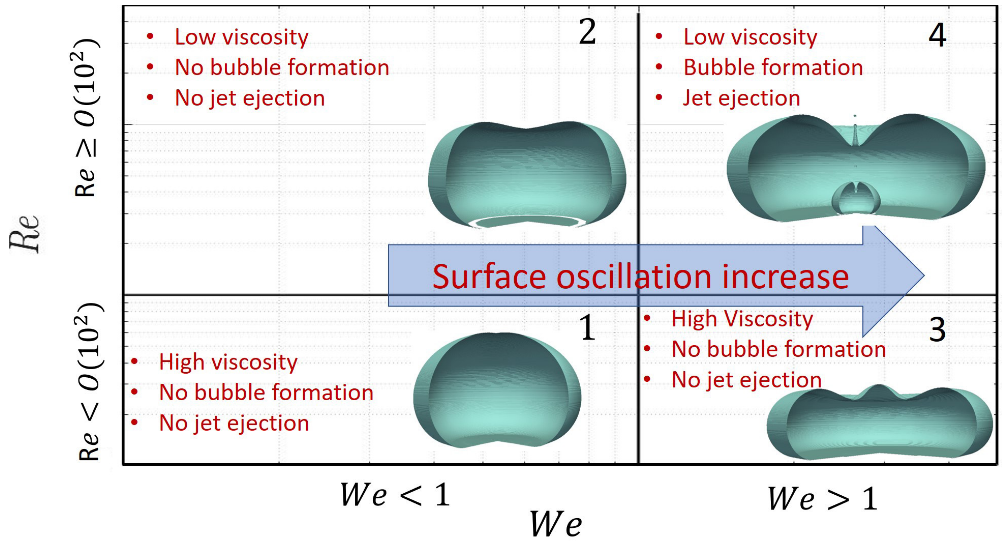

FIG. 17. A schematic view showing various types of drop-solid interactions as a function of We and Re. Physical contact with the solid surface occurs at higher values of Re while surface-oscillations-induces dissipation occurs at higher Weber numbers. Region-4, at higher values of We and Re, corresponds to bubble entrapment cases.

for high Weber number cases, and is weakly dependent on Reynolds number. Viscous dissipation is found to follow a simple scaling law given by $D \sim \mu_g V_0 R_0^2 We^{1/2} St^{1/2}$. For high We and Re, bubble entrapment can often occur as shown in figures 8 and 9. During this process, drop assumes complex shapes and involves ejection of high speed jets causing additional viscous dissipation. As the drop rises after contact, strong surface oscillations result in vigorous internal motions inside the drop. Such motions cause additional viscous dissipation which can be obtained as $(L_T - L_c)$. As is clearly evident in figure 15(b), for low We, bulk of the energy loss occurs during flight whereas at high We, bulk of the energy loss occurs during contact. This is consistent with the experiments of Kolinski *et al.*[10] carried out for $We > 1$ who noted that shear in the gas layer causes bulk of the dissipation clearly suggesting the L_c is the dominant contributor in total energy loss for high We impacts.

A key result of the paper is a detailed quantification of coefficient of restitution, r_c, shown in figure 11. Low Weber number impacts were found to have a high value of r_c whereas high Weber number impacts were found to have lower values of r_c. Satisfyingly, the simulations were found to be excellent agreement with both Kolinski *et al.*[10] and de Ruiter *et al.*[15]. For the first time, our study systematically showed how energetics of a bouncing drop subtly depends on the value of

Weber and Reynolds number. The main findings of the paper can be summarised with a simple schematic shown in figure 17.

A number of open questions remain which needs careful experiments and further numerical studies. Our simulations fail to capture dynamics if gas film thicknesses reach sub-micron levels. For high speed impacts, it is well known that gas films can easily reach nanometer ranges where both rarefaction as well as non-continuum effects become important. Their role is energetics of impact is unclear and requires further investigation. Our simulations also assume that the impact, even in wettability-dependent regimes, is axisymmetric, but a number of experiments have revealed that localised contacts first occur and the subsequent contact line motion is highly non-axisymmetric. Roughness of the substrate is another important feature which requires further investigation, mainly with regards to its effect on the coefficient of restitution. Some of these topics are currently under investigation and will be presented in future studies.

Supplementary Material

See supplementary material showing a three-dimensional evolution of bubble entrapment and escape during drop impact.

AUTHOR'S CONTRIBUTIONS

HND conceptualized, defined the scope and supervised the study, PKS carried out the numerical computations. HND and PKS analysed the data together. PKS derived the scaling laws and generated all the figures and movies. HND and PKS wrote the manuscript.

ACKNOWLEDGMENTS

PKS thanks the Ministry of Human Resource Developement for a PhD fellowship and HND thanks the Science and Engineering Research Board (SERB), Department of Science and Technology through grant ECR/2015/000086 for funding this research.

DATA AVAILABILITY

The data that support the findings of this study are available from the corresponding author upon reasonable request.

REFERENCES

[1]Akira Asai, Makoto Shioya, Shinichi Hirasawa, Takeshi Okazaki, et al. Impact of an ink drop on paper. *J. Imaging Sci. Technol.*, 37:205–205, 1993.

[2]Wilco Bouwhuis, Roeland CA van der Veen, Tuan Tran, Diederik L Keij, Koen G Winkels, Ivo R Peters, Devaraj van der Meer, Chao Sun, Jacco H Snoeijer, and Detlef Lohse. Maximal air bubble entrainment at liquid-drop impact. *Phys. Rev. Lett.*, 109(26):264501, 2012.

[3]W Jia and H-H Qiu. Experimental investigation of droplet dynamics and heat transfer in spray cooling. *Experimental Thermal and Fluid Science*, 27(7):829–838, 2003.

[4]AL Yarin. Drop impact dynamics: splashing, spreading, receding, bouncing... *Annu. Rev. Fluid Mech.*, 38:159–192, 2006.

[5]C Josserand and Sigurdur T Thoroddsen. Drop impact on a solid surface. *Annu. Rev. Fluid Mech.*, 48:365–391, 2016.

[6]L. Xu, W. W. Zhang, and S. R. Nagel. Drop splashing on a dry smooth surface. *Phys. Rev. Lett.*, 94:184505, 2005.

[7]Shreyas Mandre, Madhav Mani, and Michael P Brenner. Precursors to splashing of liquid droplets on a solid surface. *Phys. Rev. Lett.*, 102(13):134502, 2009.

[8]Madhav Mani, Shreyas Mandre, and Michael P Brenner. Events before droplet splashing on a solid surface. *J. Fluid Mech.*, 647:163–185, 2010.

[9]John M Kolinski, Shmuel M Rubinstein, Shreyas Mandre, Michael P Brenner, David A Weitz, and L Mahadevan. Skating on a film of air: drops impacting on a surface. *Phys. Rev. Lett.*, 108 (7):074503, 2012.

[10]John Martin Kolinski, L Mahadevan, and SM Rubinstein. Drops can bounce from perfectly hydrophilic surfaces. *EPL (Europhysics Letters)*, 108(2):24001, 2014.

[11]Jolet de Ruiter, Rudy Lagraauw, Dirk Van Den Ende, and Frieder Mugele. Wettability-independent bouncing on flat surfaces mediated by thin air films. *Nat. Phys.*, 11(1):48, 2015.

[12]Jolet de Ruiter, Dirk van den Ende, and Frieder Mugele. Air cushioning in droplet impact. ii. experimental characterization of the air film evolution. *Phys. Fluids*, 27(1):012105, 2015.

[13]Praveen K Sharma and Harish N Dixit. Regimes of wettability dependent and independent bouncing of a drop on a solid surface. *Submitted to J. Fluid Mech.*, 2020.

[14]D Richard and D Quéré. Bouncing water drops. *EPL (Europhys. Lett.)*, 50(6):769, 2000.

[15]Jolet Ruiter, Rudy Lagraauw, Frieder Mugele, and Dirk van den Ende. Bouncing on thin air: how

squeeze forces in the air film during non-wetting droplet bouncing lead to momentum transfer and dissipation. *J. Fluid Mech.*, 776:531–567, 2015.

[16] Denis Richard, Christophe Clanet, and David Quéré. Contact time of a bouncing drop. *Nature*, 417(6891):811–811, 2002.

[17] Ko Okumura, Frédéric Chevy, Denis Richard, David Quéré, and Christophe Clanet. Water spring: A model for bouncing drops. *EPL (Europhysics Letters)*, 62(2):237, 2003.

[18] Jan Moláček and John WM Bush. A quasi-static model of drop impact. *Phys. Fluids*, 24(12): 127103, 2012.

[19] H-Y Kim and J-H Chun. The recoiling of liquid droplets upon collision with solid surfaces. *Phys. Fluids*, 13(3):643–659, 2001.

[20] M Pasandideh-Fard, S Chandra, and J Mostaghimi. A three-dimensional model of droplet impact and solidification. *Int. J. Heat Mass Transfer*, 45(11):2229–2242, 2002.

[21] S Chandra and CT Avedisian. On the collision of a droplet with a solid surface. *Proc. R. Soc. London Ser. A*, 432(1884):13–41, 1991.

[22] Christophe Clanet, Cédric Béguin, Denis Richard, and David Quéré. Maximal deformation of an impacting drop. *J. Fluid Mech.*, 517:199–208, 2004.

[23] Stéphane Popinet. Gerris: a tree-based adaptive solver for the incompressible euler equations in complex geometries. *J. Comp. Phys.*, 190(2):572–600, 2003.

[24] Stéphane Popinet. An accurate adaptive solver for surface-tension-driven interfacial flows. *J. Comp. Phys.*, 228(16):5838–5866, 2009.

[25] Min Pack, Han Hu, D Kim, Zhong Zheng, HA Stone, and Ying Sun. Failure mechanisms of air entrainment in drop impact on lubricated surfaces. *Soft matter*, 13(12):2402–2409, 2017.

[26] Manoj Kumar Tripathi, Kirti Chandra Sahu, and Rama Govindarajan. Why a falling drop does not in general behave like a rising bubble. *Scientific reports*, 4:4771, 2014.

[27] Rogerio Manica, Evert Klaseboer, and Derek YC Chan. The impact and bounce of air bubbles at a flat fluid interface. *Soft matter*, 12(13):3271–3282, 2016.

[28] G Brant Footte. The water drop rebound problem: dynamics of collision. *J. Atm. Sci.*, 32(2): 390–402, 1975.

[29] Arvind Gopinath and Donald L Koch. Collision and rebound of small droplets in an incompressible continuum gas. *J. Fluid Mech.*, 454:145–201, 2002.

[30] Andrea Prosperetti. Viscous effects on perturbed spherical flows. *Q. A. Math.*, 34(4):339–352, 1977.